Large-Eddy Simulation of a Round Jet in Crossflow

Jörg Ziefle* and Leonhard Kleiser†
Swiss Federal Institute of Technology, 8092 Zurich, Switzerland

A numerical simulation of a round turbulent jet issuing perpendicularly into a laminar $M = 0.2$ boundary-layer crossflow is performed at a jet-to-crossflow momentum ratio of 3.3 and a jet Reynolds number of 6930. The mixing behavior of the jet in crossflow is investigated by computing the evolution of a passive scalar. The spatial discretization of the computational domain consists of a block-structured multiblock grid with 58 blocks and a total of 8.9 million cells. The NSMB (Navier–Stokes Multiblock) simulation code uses a finite-volume discretization with a skew-symmetric fourth-order central scheme and a four-stage Runge–Kutta method for time integration. To account for the subgrid scales, the approximate-deconvolution model is employed in a multiblock formulation. Of special interest is the mixing behavior of the jet with the crossflow connected with the complex vortex systems in the mixing region. Results are compared with incompressible large-eddy simulation data and experimental measurements at similar flow parameters. Significant findings comprise the study of the jet development along its trajectory, as well as the upstream influence of the crossflow into the nozzle. Furthermore, the three-dimensional temporal oscillation of the ejected jet body is investigated and an attempt is made to correlate it to the formation of vortices in the mixing region.

Nomenclature

c	=	passive-scalar concentration
D	=	nozzle diameter
d	=	difference field between nozzle and pipe flow
$E_.$	=	power density of quantity ·
f	=	frequency
H	=	Heaviside step function
L_x, L_y, L_z	=	domain size in the x, y, and z directions
M	=	Mach number
Pr	=	Prandtl number
p	=	pressure
R_{gas}	=	mass-specific gas constant
Re	=	Reynolds number
$r_{\langle \cdot \rangle}$	=	normalized maximum of quantity $\langle \cdot \rangle$ along trajectory
$\mathbf{r} = [r_x, r_y, r_z]^T$	=	center point of passive-scalar distribution above the flat wall
Sc	=	Schmidt number
St	=	Strouhal number
s	=	jet spreading rate
T	=	temperature
t	=	time
u, v, w or u_i	=	velocities in the x, y, and z directions, $i = 1, 2, 3$
V	=	volume
x, y, z or x_i	=	streamwise, spanwise, and vertical directions, $i = 1, 2, 3$
$\hat{\alpha}_{jet}$	=	threshold level for passive-scalar concentration
γ	=	isentropic coefficient, intermittency of passive-scalar concentration
ΔT	=	time interval
Δt	=	time step

$\delta_{99\%}$	=	99% boundary-layer thickness
δ^*	=	momentum thickness
ζ	=	coordinates normal to jet trajectory (defined with passive-scalar concentration) in x-z plane
η	=	coordinate normal to jet trajectory (defined with passive-scalar concentration) in x-z plane (equivalent to spanwise direction y)
λ_2	=	vortex-identification criterion
μ	=	dynamic viscosity
ξ	=	coordinate aligned with jet trajectory (defined with passive-scalar concentration)
ρ	=	density
ω_i	=	vorticity, $i = 1, 2, 3$

Subscripts

CL	=	centerline quantity within pipe or nozzle
JICF	=	mixed (jet-in-crossflow) quantity
jet	=	jet quantity
nozzle	=	quantity within jet nozzle
pipe	=	quantity of precursor pipe simulation
ref	=	reference quantity
t	=	time (ensemble) averaging
z	=	spatial averaging in z direction
$\mathcal{V}$	=	volumetric bulk quantity in pipe, $(\cdot)_{\mathcal{V}} = \int_V (\cdot)\, dV / \int_V dV$
∞	=	freestream quantity

Superscripts

T	=	vector transposition
$^-$	=	low-pass filtering
$^\vee$	=	derived quantity computed from low-pass filtered quantities
$^\sim$	=	Favre filtering

*Ph.D. Student, Institute of Fluid Dynamics, Sonneggstrasse 3; ziefle@ifd.mavt.ethz.ch. Member AIAA.
†Professor, Institute of Fluid Dynamics, Sonneggstrasse 3. Member AIAA.

I.   Introduction

THE evolution of a jet under the influence of a crossflow [jet in crossflow (JICF)] has been subject to extensive research for more than half a century. Although many earlier investigations focused on aerospace applications such as vertical and/or short takeoff and landing aircraft, steering of rockets, film cooling of turbine blades, or fuel injection into combustors, in more recent

times, ecological aspects such as plumes of smokestacks, volcanoes, or (tunnel) fires have also gained attention.

The wide occurrence of JICF-type flows goes along with a great variety of relevant flow parameters such as the Mach and Reynolds numbers and the momentum ratio of the two streams, commonly called blowing ratio. Additionally, both the jet and the boundary-layer flow can be either laminar or turbulent. The blowing ratio together with the Reynolds number exert the main influence on the type and complexity of the vortex systems that form in the mixing zone. At moderate values of these parameters, the flow in the mixing region can be characterized by a horseshoe vortex around the jet exit, shear-layer vortices above the upstream edge of the orifice, a spanwise roller at its downstream edge, and a counter-rotating vortex pair (CVP) along the jet trajectory, with upright wake vortices extending from the CVP down to the wall [1].

There exists a vast body of literature about various aspects of different JICF configurations, of which we only cite some classical works and publications that are closely related to our study. A broad overview of the history of JICF research can be gained in the comprehensive review by Margason [2]. Important measurements were carried out by Andreopoulos and Rodi [3,4], Sherif and Pletcher [5,6], Fric and Roshko [7], and Kelso et al. [1]. Other major discussions of the structure of the JICF flowfield can be found in the contributions of Smith and Mungal [8], Lim et al. [9], and Su and Mungal [10]. Numerical studies are also quite numerous. Large-eddy simulations (LES) were conducted by Yuan et al. [11–13], and Schlüter and Schönfeld [14]. Direct numerical simulations were performed recently by Muppidi and Mahesh [15,16]. Their first contribution [15] is based on a laminar jet issuing into a laminar crossflow at two relatively low velocity ratios and primarily focuses on the jet trajectory and its associated scaling laws. In the second paper [16], the authors consider a turbulent jet (but retain the crossflow laminar) and conduct detailed comparisons with the experimental data of Su and Mungal [10] at similar operating conditions. Other simulation approaches were pursued, for example, by Cortelezzi and Karagozian [17] who used vortex elements to investigate the evolution of the vortical structures in a JICF.

The parameters of the present numerical investigations are chosen akin to case 3II in Yuan's work [11], which in turn models an experiment carried out in a water channel by Sherif and Pletcher [5]. Yuan [11] aimed at studying a laminar boundary layer in combination with a turbulent jet at the moderate blowing ratio of 3.3. In accordance with Yuan, our Reynolds number is 2100 (defined with the freestream momentum, jet diameter, and dynamic viscosity at the wall), whereas Sherif and Pletcher [5] used a higher one of 4820. (Additionally, their experiments were based on a higher nominal blowing ratio of 4. Yuan's [11] lower blowing ratio is a correction for the not fully developed turbulence of the pipe flow at the orifice in the experiment.) The parameter set was chosen to yield the complex flow features commonly associated with the JICF configuration, but is still in the affordable range in terms of computational cost. The nonresolved turbulent scales are accounted for by the approximate deconvolution subgrid-scale model (ADM) [18,19] for LES.

The goals of the current study can be subdivided into two areas. Generally speaking, we would like to demonstrate the applicability of a practical LES simulation tool using ADM to a well-documented, challenging, and complex flow configuration involving massive separation. From a computational perspective, the peculiarities of the employed simulation setup are of interest. This comprises the choice of the compressible semi-industrial finite volume Navier–Stokes Multiblock (NSMB) code [20,21] with support of domain decomposition and parallelization and, particularly, our pragmatic method of generating turbulent inflow conditions for the jet nozzle. In the course of this project, a multiblock version of the ADM subgrid-scale model has been implemented into NSMB. For the first investigation of a massively separated flow with NSMB using ADM, a channel with streamwise-periodic constrictions [22,23], only a single block was necessary. The present work makes full use of the potential of the new code version by studying a challenging flow case

that requires domain decomposition and parallel computing for an efficient solution.

In the physical domain, we demonstrate the capability of our LES to yield accurate results by a comparison with the LES data of Yuan [11] and the experimental measurements of Sherif and Pletcher [5]. We extract new or rarely investigated results from the large database of simulation data for the instantaneous and the mean flow. This comprises the upstream influence of the jet into the nozzle, as well as the periodic spatial "wagging" of the ejected jet core and its connection to the formation of coherent structures in the mixing region. Other than that mentioned, the mixing behavior of the two streams and the complex vortex systems in the mixing region stand in the foreground.

The paper is organized as follows. In the next section, the studied JICF configuration will be introduced, including the computational domain and its discretization, the initial and boundary conditions chosen, and peculiarities of the simulation setup. Section III will focus on the numerical aspects of the computation. Results are presented in two parts, namely, the time-averaged data in Sec. IV and features of the instantaneous flowfield in Sec. V.

II. Flow Configuration and Simulation Methodology

Figure 1 shows a schematic of the present JICF configuration. The laminar boundary-layer profile at the upstream inlet, obtained from solving the compressible boundary-layer equations, is prescribed by Dirichlet boundary conditions. At the isothermal walls below the boundary layer and within the circular jet nozzle, which are both at the same temperature, no-slip boundary conditions are enforced. The outflow zones at the top, side, and downstream boundaries are treated with a characteristic boundary condition [24].

The jet nozzle consists of two separate and independent parts, marked (1) and (2) (white circles) in Fig. 1. The upper part (2) (white circle), which ends at the orifice, obtains its inflow data from the lower part (1) (white circle) by the usual block-coupling technique, symbolized by connection (1) (black circle). The lower part of the nozzle, however, is not coupled to the upper one but assumes streamwise-periodic boundary conditions [connection (2), black circle]. In these so-called blind blocks, an independent simulation of turbulent pipe flow is carried out concurrently with the main JICF simulation.

The flow in the boundary layer above the flat wall (3) is initialized with a properly scaled laminar boundary-layer profile and the passive scalar is set to zero. The initial data in the blind blocks for the pipe flow (1) (white circle) are obtained from an analytical solution of compressible laminar pipe flow [25] with added disturbances, so as to force a breakdown to turbulence, and a value for the passive scalar of one. For a smooth transition in the initial data, the flowfield in the
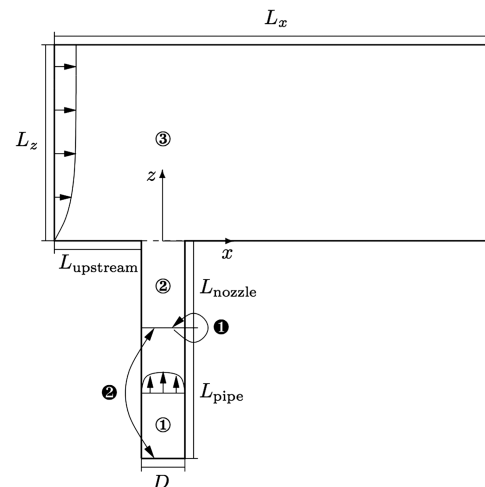

Fig. 1 Schematic of the jet-in-crossflow configuration: Turbulent pipe-flow simulation 1, nozzle 2, and boundary layer of main JICF simulation 3. Data transfer between pipe and main JICF simulations (1 and 2, black).
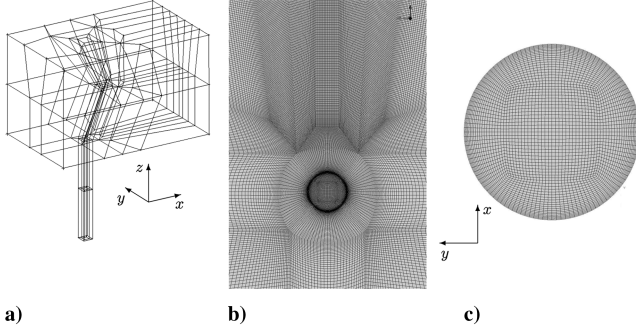
Fig. 2 Multiblock grid for the present JICF configuration: a) block topology, b) magnification of mesh near jet exit at boundary layer, and c) mesh for pipe simulation.

pipe nozzle (2) (white circle) is linearly blended toward the respective quantities in the orifice.

The current computational grid with about 8.9 million finite volume cells, depicted in Fig. 2, was generated with the commercial mesh generator ICEM CFD Hexa. Its topology, see Fig. 2a, consists of 58 structured blocks with matching interfaces. Five blocks (4.5% of the cells) comprise the pipe region (1) and another five blocks (also 4.5% of the cells) are used for the nozzle (2).

III. Numerical Discretization and Large-Eddy Simulation Method

The Navier–Stokes multiblock code [20,21] employed for this investigation is a block-parallel, cell-centered, compressible finite volume solver for structured grids. NSMB incorporates a number of different Reynolds-averaged Navier–Stokes and LES models, as well as spatial (central and upwind) discretization schemes with an accuracy up to fourth order (fifth order for upwind schemes). Technical details about NSMB can be found in [26], and examples of complex flows simulated with NSMB have been published in [27–29].

The simulation of the present study is carried out with a skew-symmetric central spatial discretization of fourth-order accuracy, for which the intrinsic properties contribute to accuracy and numerical stability by reducing aliasing errors [30,31]. The Navier–Stokes equations are integrated in time with a standard four-stage Runge–Kutta scheme (which is of fourth-order accuracy for linear equations). To facilitate statistical sampling, the time step was held constant at $\Delta t = 0.7 \times 10^{-3}$ time units $D/\tilde{u}_\infty$. This corresponds to a Courant–Friedrichs–Lewy number of approximately 1.5, which is slightly more than half of the linear stability limit of the employed time-integration scheme.

To account for the fact that the experiment [5] has been carried out in a water channel, a perfect gas with an isentropic coefficient of $\gamma = 1$ and a Prandtl number of $Pr = 7$ is used. Jet buoyancy effects are not considered in this flow, corresponding to an infinite Froude number. The dependency of the dynamic viscosity on the temperature is modeled with a power law [32]

$$\check{\mu}(\check{T})/\check{\mu}_{\text{ref}} = (\check{T}/\check{T}_{\text{ref}})^{0.7} \tag{1}$$

where the temperature $\check{T}_\infty$ and dynamic viscosity $\check{\mu}_\infty$ in the freestream (which have the same values as at the isothermal walls) are employed as reference conditions. Other quantities used for the nondimensionalization are the pipe diameter D and the freestream momentum in the boundary layer $(\bar{\rho}\tilde{u})_\infty$. The freestream pressure needed for the normalization of the pressure can be expressed as $\check{p}_\infty = 1/(\gamma M_\infty^2)$.

The main components of the approximate deconvolution model, which is employed here as subgrid-scale model for LES, are the direct computation of the nonlinear fluxes with an approximation of the unfiltered state vector, obtained by an approximate deconvolution (defiltering) procedure [18], and a relaxation term employed for regularization [19]. The approximate deconvolution is based on a

truncated series expansion of the inverse LES filter, leading to an approximate deconvolution filter defined by a linear combination of the repeatedly filtered state vector. For simplicity and a reduced computational effort, we employ a constant relaxation coefficient $\chi = 1/\Delta t$ in the relaxation term.

To investigate the mixing of the two streams, the evolution of a passive scalar has been implemented into the flow solver via a three-dimensional advection-diffusion equation, in which the Schmidt number Sc (chosen equal to the Prandtl number) determines the relation between convection and diffusion.

The volumetric mass-flow rate

$$(\bar{\rho}\tilde{w})_\mathcal{V} := \int_\mathcal{V} \bar{\rho}\tilde{w} \, dV / \int_\mathcal{V} dV$$

in the independent pipe simulation (region 1, white circle, in Fig. 1) is maintained exactly by a forcing term representing a mean pressure gradient, which is implemented as a spatially constant but temporally varying volume force acting in the streamwise z direction [33]. The characteristic geometry and flow parameters are summarized in Table 1.

IV. Mean-Flow Results

In the following, the structure of the mean flowfield will be discussed. Time-averaging was performed by sampling the instantaneous flowfield every 30 time steps during a time interval of more than 250 time units $D/\tilde{u}_\infty$. This averaging time is significantly longer than in the reference computation [11], where available computational resources limited sampling to 80 time units. However, our statistics were still found to be not perfectly symmetric, especially in the far field downstream of the jet exit, where the flow is highly unsteady and irregular.

The computation was carried out in parallel on four processors of a NEC SX-8 vector machine, using more than 3000 CPU hours (including initial transients). During time averaging, 12 GB of memory were necessary. One instantaneous flowfield (including mesh and restart data) consumes 1.4 GB of disk space, whereas the time-averaged flowfield (73 scalar quantities) requires 5.9 GB of disk space. The total accumulated data (including a series of instantaneous flowfields for animation and frequency analysis purposes) comprise approximately 700 GB.

A. Jet Trajectory

The jet trajectory is one of the most important characteristics of a JICF. Naturally, its determination is to some extent a matter of definition. Here, we compute the jet trajectory in three different ways that are commonly used in the literature [11]. As the first possibility, see Fig. 3a, the streamline of the mean flowfield through the center of the jet nozzle ($[x, y, z]^T = \mathbf{0}$) marks the jet trajectory. Additionally, the streamlines starting at the upstream and downstream edges of the jet nozzle are shown as an approximation of the jet boundary in the center plane. Secondly, as depicted in Fig. 3b, the trajectory can be defined as the locus through all points with maximum scalar concentration in the center plane $y = 0$. Alternatively, the maximum velocity magnitude can be used as a defining quantity, as shown in Fig. 3c.

All trajectories exhibit generally good agreement with the computational results of Yuan [11], even though the sensitivity to the particular method of determination is quite strong for the latter two

Table 1 Geometric and flow parameters (cf. Fig. 1)

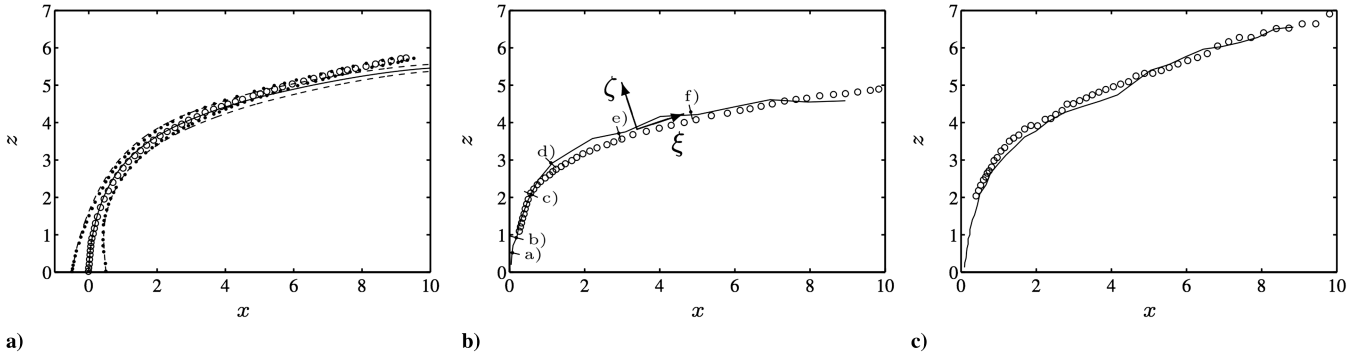|					
L_x	=	16	$R = (\bar{\rho}\tilde{w})_\mathcal{V}/(\bar{\rho}\tilde{u})_\infty$	=	3.3
L_y	=	10	$Re_{\text{jet}} = (\bar{\rho}\tilde{u})_\infty D/\check{\mu}_\infty$	=	2100
L_z	=	10	$Re_{\text{jet}} = Re_{\text{pipe}} = (\bar{\rho}\tilde{w})_\mathcal{V} D/\check{\mu}_{\text{wall}}$	=	6930
L_{upstream}	=	5.5	$Re_{\text{BL}} = (\bar{\rho}\tilde{u})_\infty \delta_{99\%}/\check{\mu}_\infty$	=	1050
L_{nozzle}	=	5	$Re_{\delta^*\text{BL}}|_{\text{inlet}}$	=	309.28
L_{pipe}	=	5	$M_\infty = \tilde{u}_\infty/\sqrt{\gamma R_{\text{gas}}\check{T}_\infty}$	=	0.2
D	=	1	$\delta_{99\%}/D$	=	0.5

Fig. 3 Jet trajectories determined with a) streamlines, b) maximum passive-scalar concentration, and c) maximum velocity magnitude. Solid lines show present LES, circles show LES of Yuan [11], dashed lines show bounding streamlines in present LES, and dotted lines show bounding streamlines in LES of Yuan. The symbols a–f in Fig. 3b mark the locations of the trajectory-normal cross sections displayed in Figs. 7–10. The coordinate system with directions ξ, η (spanwise direction, not visible), and ζ locally follows the passively scalar trajectory.

methods. Some larger deviation occurs for the streamline trajectory downstream of the region of high curvature, where our trajectory lies below the one determined by Yuan and also ascends at a lower slope. Our passive-scalar trajectory in Fig. 3b also bends slightly later and with a larger radius. However, because a comparison of the vertical mean scalar-concentration profiles at different streamwise positions in this area reveals good agreement of the scalar maximum locations (as shown in Fig. 4), we attribute the observed differences mainly to discrepancies in the determination of the trajectory.

As commonly observed, the trajectory computed with the maximum velocity magnitude lies above the one defined by the maximum scalar concentration. The reasons for this will be discussed in Sec. IV.D. The slight irregularity of the data points for the trajectories of the maximum scalar concentration and velocity magnitude for $z > 3$ can be explained by the high level of mixing and off-center-plane effects in combination with a slight asymmetry of the mean flowfield in this region. The higher unsteadiness this far downstream would require longer sampling times for the statistics to fully converge and thus reduce the uncertainty and improve the symmetry in the time-averaged flowfield. A similar problem was experienced with the streamline trajectory, where the spanwise velocity $\langle \tilde{v} \rangle$ had to be explicitly set to zero to avoid a deflection of the streamline off the center plane and into the influence of the counter-rotating vortex pair.

B. Three-Dimensional Flowfield and Stationary Vortex Structures

Perhaps the most illustrative insight into the complex flow features associated with the deflected jet can be gained by studying streamlines of its mean velocity field. Note that this allows one to investigate primarily the stationary vortex systems of the JICF, such as the horseshoe vortex and the spanwise roller at the downstream edge of the jet exit. The traveling vortices, in particular, the wake vortices and the shear-layer vortices, can only be seen in visualizations of the instantaneous flowfield, which will be discussed in Sec. V.

In Figs. 5a and 5b, we display two sets of streamlines originating from the jet nozzle and from the crossflow. The "crossflow streamlines" start from a spanwise line within the boundary layer upstream of the jet exit at 10% boundary-layer thickness. The "nozzle streamlines" are seeded across the jet nozzle throughout the two diameters aligned with the x and y axes.

Following the crossflow streamlines, we observe their deflection around the jet exit, as the jet obstructs their downstream path, and the creation of a horseshoe vortex (see marker 1). The circular part of the horseshoe vortex wrapping around the orifice cannot be directly observed in Figs. 5a and 5b. It is, however, indicated by the lack of crossflow streamlines close to the jet exit. In both views, we can clearly recognize the bundling of the outer streamlines to form the two legs of the horseshoe vortex (2). The streamlines close to the center plane pass under the other streamlines. After a wide circle around the jet exit, they finally join the horseshoe legs (2) or move downstream parallel to it.

At the downstream edge of the jet exit, a spanwise vortex (3) caused by the roll up of the jet shear layer induces negative streamwise velocities near the wall. Therefore, some of the boundary-layer streamlines within the horseshoe legs are forced to move upstream toward the jet exit. There, they fall into the upward influence of the emerging jet and its counter-rotating vortex pair (5). Note that the backflow induced by the spanwise roller (3) reaches as far downstream as 2.5 hole diameters from the jet exit.

The path of the streamlines emanating from the jet nozzle is more regular. The inner ones follow more or less the jet trajectory, whereas the ones at the spanwise edges of the jet are subject to the influence of a stationary inclined vortex pair (4) above the lateral sides of the jet exit. Farther downstream, those hanging vortices form the counter-rotating vortex pair [CVP (5)], which is clearly visible in the front view (Fig. 5a).

A different presentation of the stationary vortex structures is possible by visualizing isocontours of the vortex-identification criterion [34] $\check{\lambda}_2$, computed from the time-averaged flowfield, see Fig. 5c. Here, we get a better overview of the spatial location of the round part of the horseshoe vortex (1) around the jet exit hole, the counter-rotating vortex pair (5), and the two hanging vortices (4). Additionally, the two legs of the horseshoe vortex (2) appear rather clearly.

C. Flow Data in Center Plane

Figure 6 shows contour visualizations of the mean-flow quantities in the center plane of the JICF $y = 0$. For brevity, only a part of the jet nozzle is depicted. The mean streamwise velocity $\langle \tilde{u} \rangle$ in Fig. 6a illustrates several flow features of the mixing region. The jet represents an obstacle to the oncoming boundary-layer flow, which consequently has to move around the ejected jet core, resulting in two stagnation regions just upstream and downstream of the jet trajectory. In the near-wall zone downstream of the jet exit, high negative velocities (of the same magnitude as the freestream velocity) occur due to the already mentioned spanwise vortex originating from the separated jet shear layer. Farther away from the wall, in the strongly curved region of the jet trajectory, streamwise velocity is induced by the inclined counter-rotating vortex pair. High positive velocities (nearly 1.5 times the freestream velocity) are observable on the jet trajectory at some distance away from the exit. Here, the boundary layer has deflected the vertical jet toward the horizontal direction, thus its high velocities obtain a streamwise component. As expected, the streamwise velocity in the nozzle region is negligible.

The described flow features can be further witnessed in the plot of the mean wall-normal velocity $\langle \tilde{w} \rangle$ (Fig. 6b). Additionally, we recognize two distinct areas of elevated vertical velocity. The more upright one is a direct effect of the jet fluid deflected by the crossflow. The more horizontal branch is a consequence of fast jet fluid being convected downstream by the hanging vortices above the lateral sides of the jet exit.

Some stationary vortical structures are well observable in the contour of the mean spanwise vorticity component $\langle \check{\omega}_y \rangle$ in Fig. 6c.
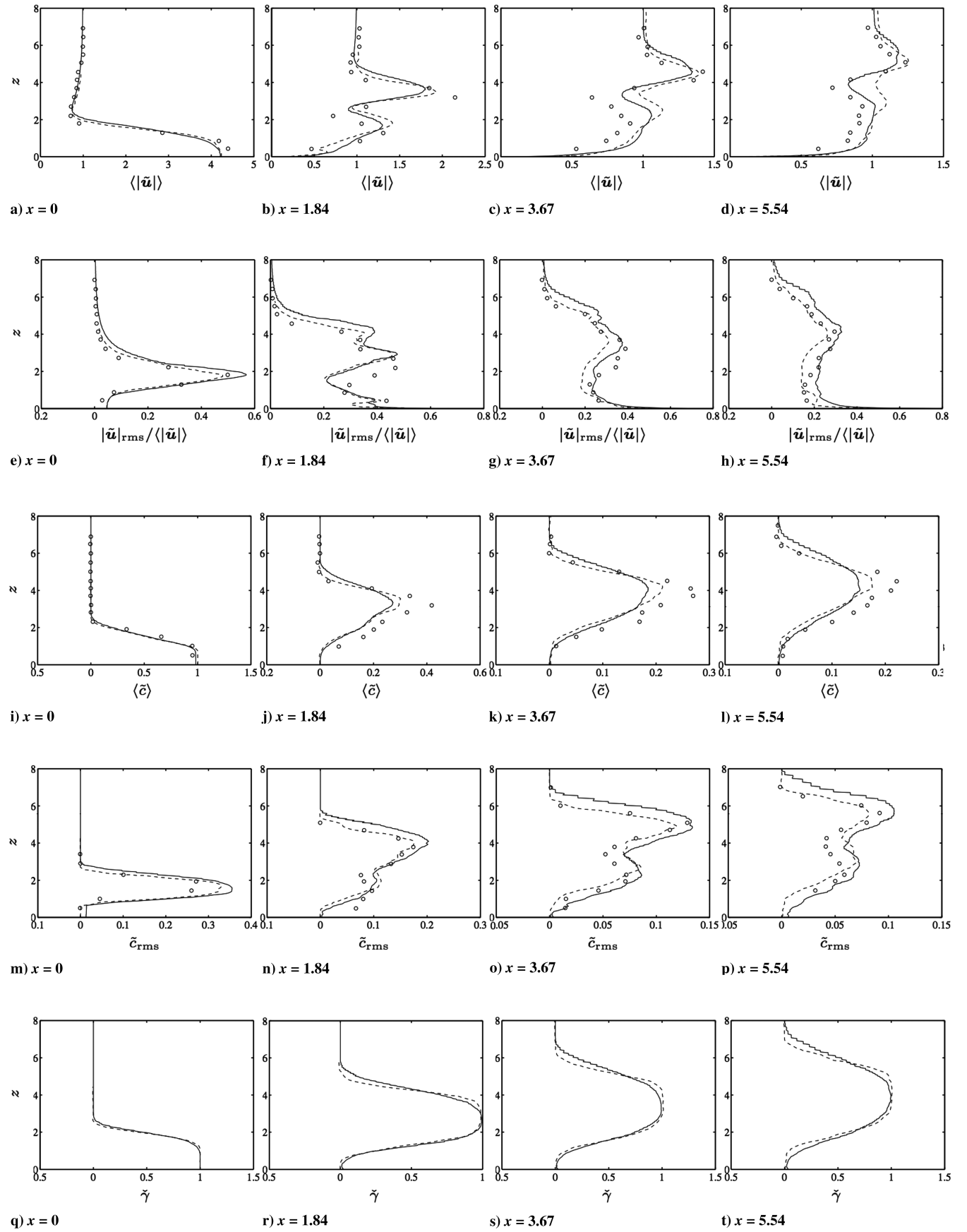
Fig. 4 **Vertical profiles of time-averaged quantities at four streamwise positions in the center plane $y = 0$: a–d) mean velocity magnitude $\langle|\tilde{u}|\rangle$, e–h) normalized rms fluctuations of the velocity magnitude $|\tilde{u}|_{\mathrm{rms}}/\langle|\tilde{u}|\rangle$, i–l) mean passive-scalar concentration $\langle\tilde{c}\rangle$, m–p) rms fluctuations of the passive-scalar concentration $\tilde{c}_{\mathrm{rms}}$, and q–t) scalar intermittency $\check{\gamma}$. Solid lines indicate present LES, dashed lines indicate LES of Yuan [11], and circles indicate the experiment of Sherif and Pletcher [5].**
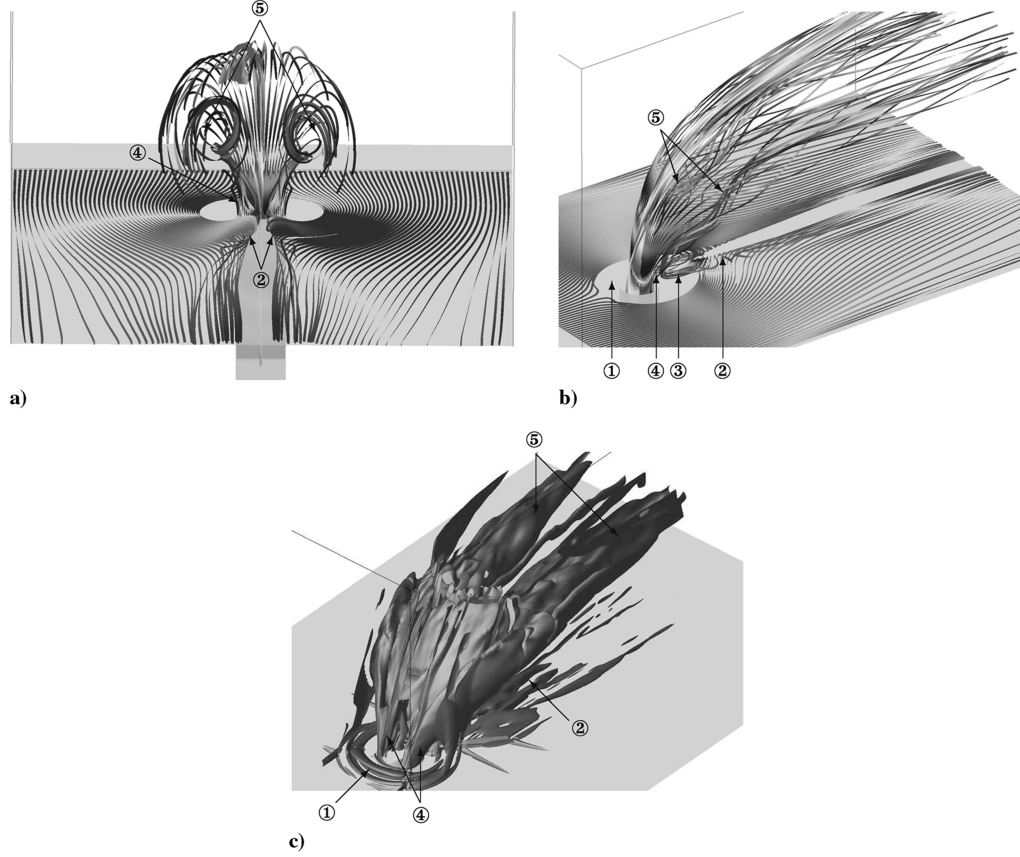
Fig. 5   Visualization of the mean-flow vortex structure. Streamlines of the mean velocity field (displayed as ribbons twisted by the local average vorticity): a) front view looking upstream, b) lateral view. c) Vortex-identification criterion $\check{\lambda}_2$ applied to mean flowfield.

Note that the maximum vorticity magnitude is more than 10 times larger than the value range indicated in the legend. Those very high values occur in the separating jet shear layer near the jet nozzle. Also, the zero spanwise vorticity contour line has been omitted for clarity reasons, as it is very noisy and has a spotty distribution throughout the center plane. The nearly unperturbed laminar boundary layer upstream of the jet nozzle and the boundary layers in the turbulent pipe nozzle are governed by the typical vorticity distribution due to mean shear. The boundary layer within the jet nozzle separates and forms a shear layer after being ejected, resulting in high vorticities in the near field along the trajectory. Just downstream of the jet exit, the spanwise roller is visible and, above the upstream edge of the nozzle, the horseshoe vortex can be spotted by the elevated vorticity levels within the boundary layer. An increasing and regularly formed distribution of vorticity magnitude in the near-wall region farther downstream of the nozzle indicates the development of a new boundary layer.

Figure 6d shows the mixing behavior of the JICF by means of the mean passive-scalar concentration $\langle \tilde{c} \rangle$. Just above the jet nozzle, where the crossflow is not able to displace the jet fluid, a pyramidlike area with pure jet fluid exists. This slightly downstream-oriented jet core is much shorter than those of vertical jets without crossflow [35]. After the jet core closes, the scalar concentration and its gradient diminish rather quickly along the jet trajectory due to mixing with oncoming boundary-layer fluid. Jet fluid is also removed from the jet core region, for example, by the hanging vortices in the nozzle region and farther downstream by the counter-rotating vortex pair, as well as by passing boundary-layer fluid (as shown in Fig. 7). Therefore, elevated scalar-concentration levels are observable in the wake of the jet.

In Fig. 6e, the contours of the so-called scalar intermittency $\check{\gamma}$ are depicted. This quantity is derived from the passive-scalar concentration $\tilde{c}$ and represents the fraction of time during which the scalar concentration locally exceeds a certain threshold value $c_{\text{jet,min}}$,

$$\gamma(x, y, z) := \frac{1}{\Delta T} \int_{t_0}^{t_0 + \Delta t} H[c(x, y, z) - c_{\text{jet,min}}] \, dt \qquad (2)$$

where H denotes the Heaviside step function. Following Yuan [11], the threshold was chosen as $\tilde{c}_{\text{jet,min}} = 0.01$ which is meant to distinguish between jet and boundary-layer fluid. Unlike the scalar concentration, which diminishes quite quickly along the jet trajectory, the intermittency levels remain high and regular along the trajectory. Thus, the intermittency gives a more adequate picture of the spatial spreading of the jet fluid. The lower low-valued contour lines run nearly parallel to the wall because the boundary-layer fluid, which has circumscribed the jet core, forms a layer which cannot easily be entrained by the jet. The upper ones seem to ascend with constant slope after the high-curvature bending of the jet trajectory, which agrees with the constant spreading rate observed in the literature [36,37]. Even regions which are quite distant from the jet trajectory are reached by fluid originating from the jet during significant fractions of time. This is mainly an effect of the strong vortex systems like the hanging vortices and the CVP, which are able to transport jet fluid far away from its core. Note that the 90% intermittency contour lines roughly correspond to the 10% contour lines of the passive-scalar concentration in Fig. 6d.

The contour of the normalized mean pressure $\langle \check{p} \rangle / \check{p}_\infty$ in Fig. 6f mainly exhibits three features. Viscous drag causes the pressure to drop continuously in the jet nozzle. Upstream of the vertical part of the jet trajectory, a stagnation region is visible in the form of elevated pressure levels, which even extends slightly into the jet nozzle. The pressure minimum above the downstream edge of the jet exit is typical for a wake region and intensified by the standing spanwise roller [9].

D.   Development of Jet Along Trajectory

1.   Contours in Cross Sections Normal to Jet Trajectory

The spatial development of the jet and its counter-rotating vortex pair along the jet trajectory can be well observed by studying
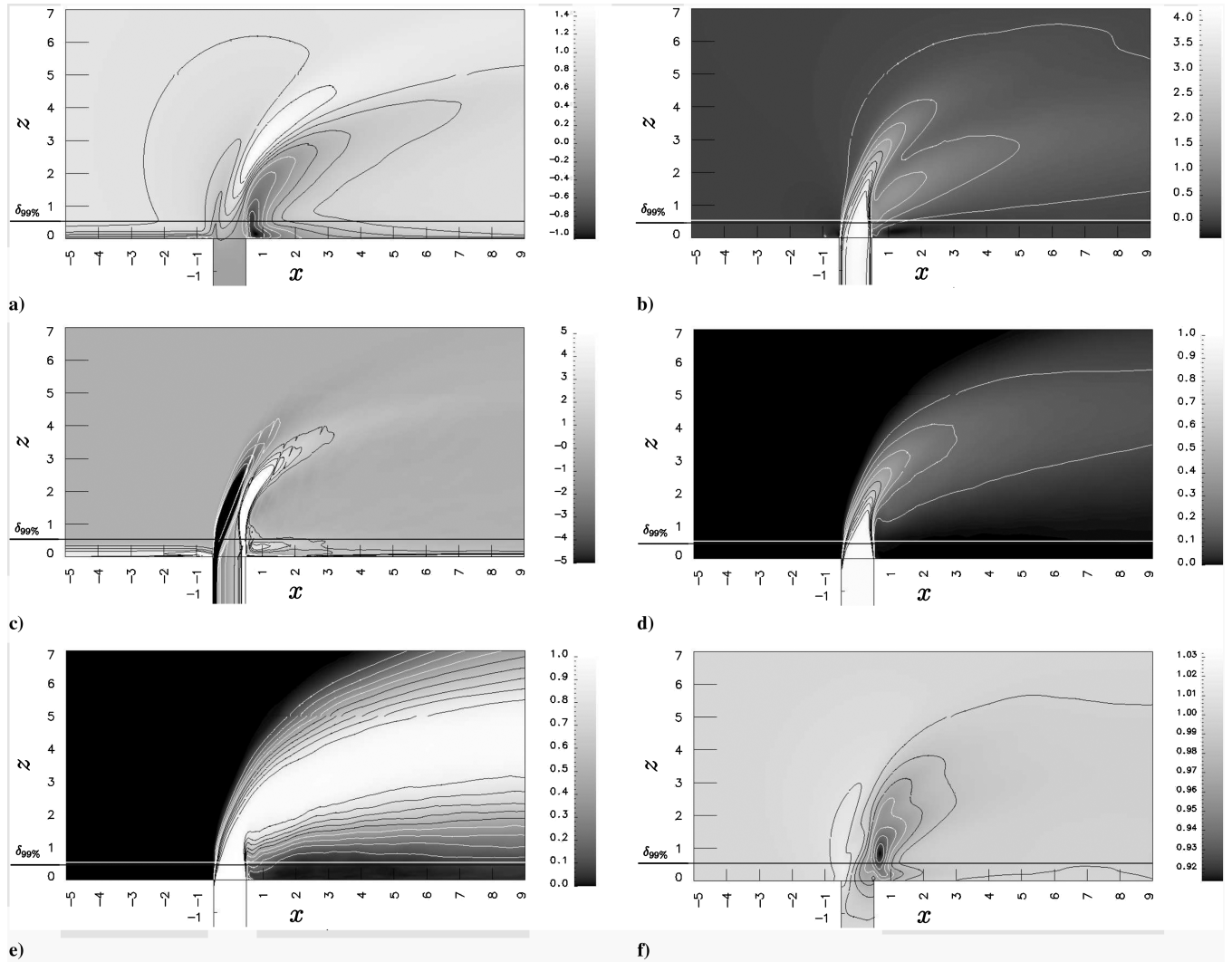
Fig. 6   Visualization of mean-flow data in the center plane $y = 0$: a) streamwise velocity $\langle \tilde{u} \rangle$, b) vertical velocity $\langle \tilde{w} \rangle$, c) spanwise vorticity $\langle \breve{\omega}_y \rangle$ (note the reduced value range of the legend as mentioned in the text), d) passive-scalar concentration $\langle \tilde{c} \rangle$, e) passive-scalar intermittency $\breve{\gamma}$, and f) normalized pressure $\langle \breve{p} \rangle / \breve{p}_\infty$. Also shown are 10 equidistant contour intervals (i.e., nine contour lines) ranging from the minimum to the maximum values indicated in the respective legends.

contours of the mean flowfield in planes normal to the jet trajectory, see Figs. 7–10. The positions indicated in the captions denote the distance of the center of the cross section along the scalar trajectory and have also been marked in Fig. 3b.

In the first series of contours, Fig. 7, we consider the mean passive-scalar concentration $\langle \tilde{c} \rangle$. This allows to observe the deformation of the originally circular jet cross section and its mixing with the boundary-layer fluid. In the first position, Fig. 7a, the hanging vortex pair has already changed the appearance of the contour at the downstream edge of the jet. Additionally, as soon as the jet exits the nozzle, its upstream face is compressed by the perpendicularly flowing boundary layer. At the same time, as the boundary-layer fluid is forced to move around the jet, it carries away jet fluid from the sides of the jet into the spanwise and downstream directions. This creates two effects: the jet core widens up in the spanwise direction and two "arms" of elevated scalar concentration appear downstream of the lateral sides of the jet. Also, the scalar gradient is large on the compressed upstream edge, but much smaller in the two lateral arms. These mechanisms are clearly visible in Figs. 7b and 7c. The jet fluid located on the downstream edge of the jet near the center plane is largely unaffected by the passing boundary layer. Thus, its scalar gradient is maintained at a high level for a considerable distance along the trajectory, see Figs. 7c and 7d. Additionally, the orientation of the counter-rotating hanging vortices and later the CVP contribute to the conservation of the high scalar gradients in this region. Under the continual rotational influence of the CVP in combination with

boundary-layer entrainment on the upstream jet edge, the originally contiguous region of highest cross-sectional scalar concentration is separated into two zones with lower scalar concentration in the center plane, see Figs. 7e and 7f.

Two more effects are noteworthy. Because of the mixing of the jet with the crossflow, the maximum scalar concentration decreases continually (note the varying value range of the legend) (cf. the next section). The same is valid for the scalar-concentration gradient. As the jet exits the nozzle, high gradients are observable, due to the two streams still being basically unmixed. Through convective mixing and diffusion, the gradients decrease rather quickly downstream.

Figure 8 shows the isocontours of the vorticity component aligned with the trajectory $\langle \breve{\omega}_\xi \rangle$ in the same cutting planes as in Fig. 7. The hanging vortices above the spanwise edges of the jet exit hole are clearly recognizable in form of two C-shaped areas of high vorticity in Figs. 8a and 8b. Farther downstream, as evident by the elliptical appearance of the vortex pair in the next position $\xi = 2$, they eventually turn into the counter-rotating vortex pair. As the CVP develops along the jet trajectory, the maximum vorticity decreases due to the deceleration and spreading of the jet, as well as (to a smaller extent) viscous and turbulent effects. Furthermore, the shape of the two vortices changes in such a way that vorticity accumulates in the lower half of each vortex, see Figs. 8e and 8f.

The contours of the velocity magnitude $\langle |\tilde{u}| \rangle$ in planes normal to the jet trajectory (Fig. 9) explain why the maximum scalar-concentration trajectory runs lower than the maximum velocity
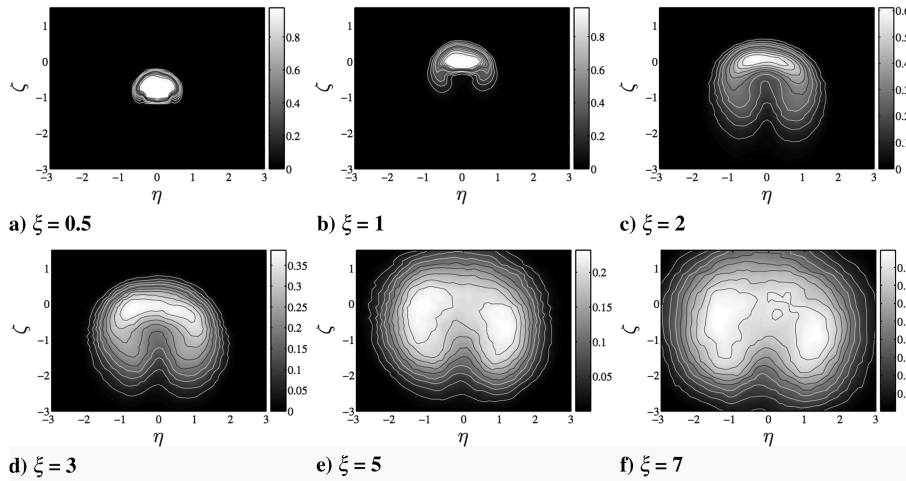
Fig. 7   Contours of the mean passive-scalar concentration $\langle \breve{c} \rangle$ **in planes normal to jet trajectory. Contour legend for Figs. 7–10: dashed lines show 10 equidistant contour intervals (i.e., nine negative contour levels) from minimum of value range to zero; thin solid lines show 10 equidistant contour intervals from zero to maximum of value range, thick solid lines show zero contour level. The positions of** ξ **indicate intersections of cut-planes and scalar trajectory and are marked in Fig. 3b. The spanwise coordinate is denoted by** $\eta \equiv y$**, and** ζ **is normal to** ξ **and lies in the** x-z **plane.**
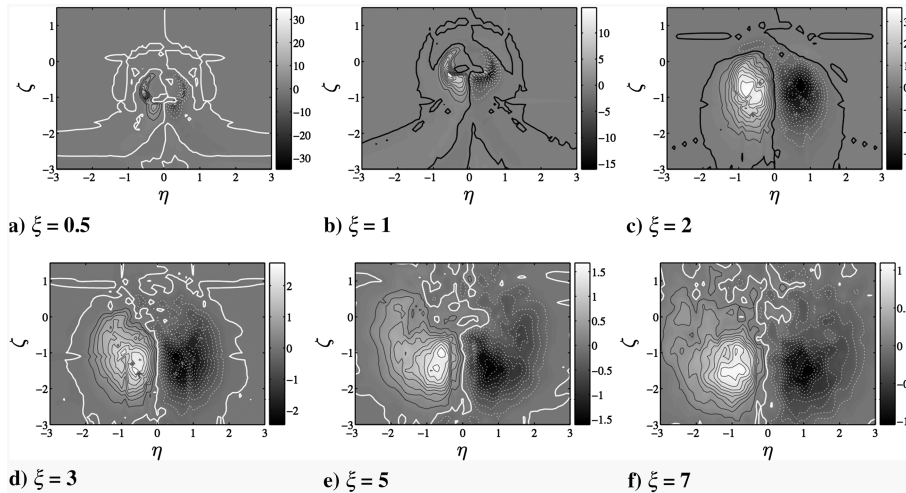

Fig. 8   Visualization of the mean out-of-plane vorticity component $\langle \breve{\omega}_\xi \rangle$ **in planes normal to jet trajectory. Contour legend,** ξ **positions, and** (η, ζ) **coordinates as in Fig. 7.**

trajectory after some distance along the trajectory (cf. Figs. 3b and 3c). After the jet is ejected into the crossflow, both the maximum velocity and the scalar concentration are highest in a region near the center of the jet core. Thus, both trajectories still stay closely together. Under the continual influence of the crossflow and the strong vortex systems, and due to dissipation, an increasing amount of jet fluid with high scalar concentration and velocity magnitude is carried away from the jet core. Although the crossflow can only compress the appearance of the scalar distribution and reduce its magnitude (cf. Fig. 7), it exerts a quite different effect on the velocity magnitude. As the jet is deflected in the downstream direction, an increasing amount of boundary-layer fluid entrains it and contributes to its velocity magnitude. This entrainment mainly happens at the windward face of the jet. Hence, the velocity maxima deviate from the location of maximum scalar concentration toward the upstream direction. Furthermore, the maximum velocities occur in the center plane $y = 0$, whereas the passive-scalar maxima lie off the center plane (cf. Fig. 7). The influence of the crossflow on the jet is already evident in the first few positions (frames of Figs. 9a–9c). Here, as discussed for the passive-scalar concentration, the boundary-layer fluid is forced to move around the jet, compressing the jet core and building two lateral arms of high-velocity fluid downstream of it. Under the influence of the CVP, the arms grow and bend toward the center plane, leading to a more pronounced appearance in Figs. 9d–9f.

Note that, especially at the last three stations, the velocity maxima are not located in the center plane, but slightly to the left side, and the contours appear somewhat spotty. As discussed before, although our averaging time interval has been chosen more than 3 times as long as in the reference results of Yuan [11], it is still not long enough for completely converged and symmetric statistics. This suggests that the consideration of off-center-plane effects in the determination of the trajectory would render the quantification of the jet trajectory more robust. For example, a procedure similar to the determination of the center of mass for a density distribution on a surface could be used to take off-center-plane effects into consideration. However, we refrained from doing so to maintain comparability with reference data.

The final set of cross-sectional contours in Fig. 10 depict the normalized mean pressure $\langle \breve{p} \rangle / \breve{p}_\infty$. Just upstream of the jet trajectory, a stagnation region is visible by elevated pressure levels. The two hanging vortices above the jet exit and the CVP appear as initially rather strong pressure minima for $\xi = 0.5$, $\xi = 1$, and $\xi = 2$. As the CVP loses vorticity along its trajectory (cf. Fig. 8), the pressure differences also assimilate. A striking feature in the first plot, Fig. 10a, is the existence of an additional pair of low-pressure zones downstream and closer to the centerline than the hanging vortices. As an investigation of the three-dimensional flowfield reveals, and as is also evident from Fig. 6f, they belong to the
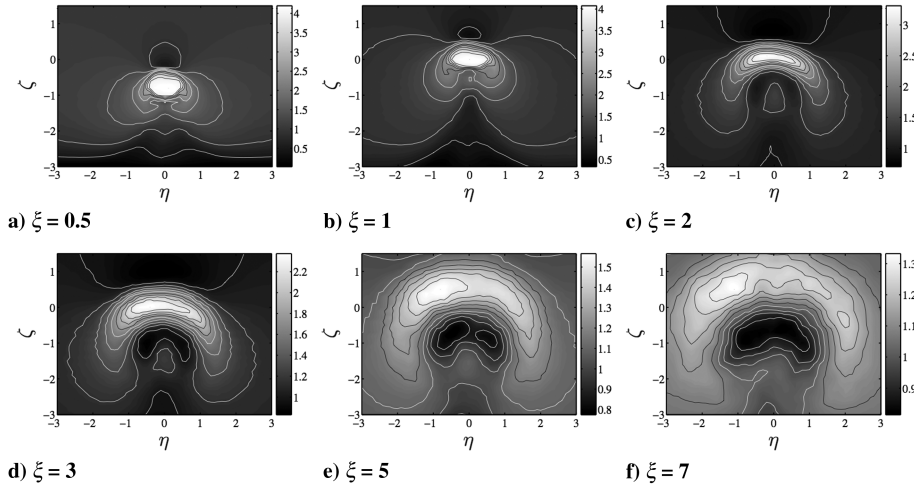
Fig. 9   Contours of the mean velocity magnitude $\langle |\tilde{u}| \rangle$ in planes normal to jet trajectory. Contour legend, ξ positions, and (η, ζ) coordinates as in Fig. 7.
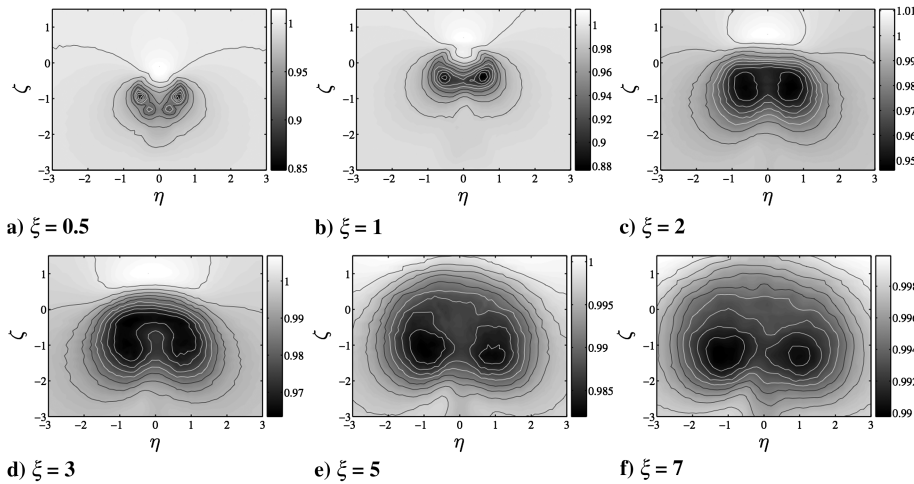

Fig. 10   Contours of the normalized mean pressure $\langle \breve{p} \rangle / \breve{p}_\infty$ in planes normal to jet trajectory. Contour legend, ξ positions, and (η, ζ) coordinates as in Fig. 7.

upward-bent spanwise ends of the strong spanwise roller downstream of the jet nozzle.

2.   Jet Spreading and Decay of Momentum and Passive-Scalar Concentration

We now use the cross sections normal to the jet trajectory to obtain a more quantitative description of the jet development along its trajectory. To distinguish between jet fluid and crossflow fluid, it is common to define a threshold level of the passive-scalar concentration $\tilde{c}_{\text{jet,min}}$. If the local passive-scalar concentration lies below this threshold level, the fluid is considered to be pure crossflow fluid, otherwise it is assumed to be a mixture between jet and crossflow fluid. [This assumes that the value range of the passive-scalar concentration varies from zero (pure crossflow fluid) to unity (pure jet fluid).] With this criterion, the jet spread rate s along the trajectory is determined as the fraction of area covered by jet fluid. Because of the continual downstream dilution of the jet, the preceding absolute threshold level is replaced by a relative definition, $\tilde{c}_{\text{jet,min}} = \alpha_{\text{jet,min}} \tilde{c}_{\text{max}}$, with $\tilde{c}_{\text{max}}$ denoting the local, that is, cross-sectional maximum passive-scalar concentration, and $\alpha_{\text{jet,min}}$ being the relative threshold level similar to the absolute one described previously. Using the Heaviside step function H, the spread rate can be expressed as

$$s(\xi; \alpha_{\text{jet,min}}) := \frac{\int_\zeta \int_\eta H(\tilde{c} - \alpha_{\text{jet,min}} \tilde{c}_{\text{max}})\, d\eta\, d\zeta}{\int_\zeta \int_\eta d\eta\, d\zeta} \quad (3)$$

Figure 11a displays the spread rate for four different threshold levels and compares our result to the data of Yuan [11]. The agreement is very good for all four curves, with only the first few data points showing small deviations. The jet spread rates grow fast in the initial part of the trajectory just downstream of the jet exit. At $\xi \approx 2$, at the end of this more vertical part, the jet trajectory begins to bend horizontally (cf. Fig. 3b) and the spread rates continue to grow at a considerably lower rate. This location is somewhat downstream of the end of the jet core, as evident from Figs. 6d and 7c, as well as from Fig. 11b.

Because of the mixing of the jet with the crossflow fluid, both the passive-scalar concentration and the contravariant (i.e., trajectory-parallel) velocity decay along its trajectory (cf. Figs. 7 and 9). In Figs. 11b and 11c, we investigate the decay of those two mean quantities $\langle \cdot \rangle$ with the ratio of their local maxima (i.e., in dependence on the trajectory coordinate ξ) to their maxima in the orifice plane ($\xi = 0$):

$$r_{\langle \cdot \rangle}(\xi) := \frac{\max\limits_{\eta, \zeta} \langle \cdot \rangle(\xi)}{\max\limits_{\eta, \zeta} \langle \cdot \rangle(\xi = 0)} \quad (4)$$

As common in literature, we study both the cross-sectional decay (all transversal locations in a plane $\xi = \text{const}$ are considered) and the centerline decay (only centerline locations $\xi = \text{const}, \eta = 0$ are used).

The extent of the jet core can be quantified from Fig. 11b, which shows the decay of the maximum passive-scalar-concentration ratio
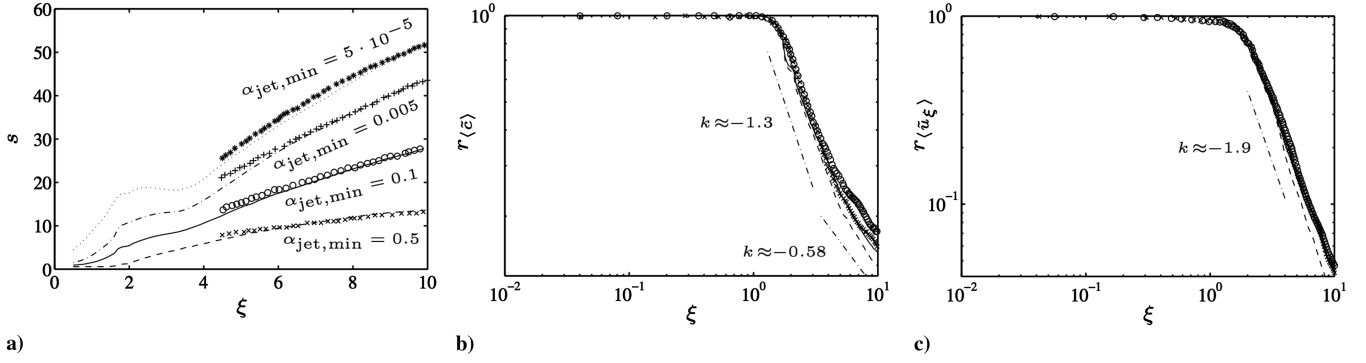
Fig. 11 Quantification of the jet development along its trajectory: a) Jet spread rates $s(\xi; \alpha_{jet,min})$ for four threshold levels $\alpha_{jet,min}$ of the passive-scalar concentration. Lines indicate present simulation, symbols indicate LES of Yuan [11]. b) Development of normalized mean passive-scalar-concentration maximum $r_{\langle \tilde{c} \rangle}$ along jet trajectory. Lines indicate present simulation (lines: all transverse locations, dashed lines: center plane only), symbols indicate LES of Yuan (circles: all transverse locations, crosses: center plane only). Dashed-dotted lines show empirical decay behavior $r_{(\cdot)}(\xi) \sim \xi^k$ from literature. c) Development of normalized mean trajectory-parallel velocity maximum $r_{\langle \tilde{u}_\xi \rangle}$ along jet trajectory (same legend as in Fig. 11b).

$r_{\langle \tilde{c} \rangle}$. This quantity remains undiluted until $\xi \approx 1.2$. At this point, the jet core closes, which is also evident from Fig. 6d, and the passive-scalar concentration decays fast according to a power law, that is, $r_{\langle \tilde{c} \rangle} \sim \xi^k$ with exponent $k \approx -1.3$ [11]. Farther downstream, where the jet spreads faster again (cf. Fig. 11a at $\xi \approx 4$), the decay rate decreases to an approximate exponent of $k \approx -0.58$. Both the beginning of the decay as well as the initial decay rate agree well with the data of Yuan. Only in the later part of the trajectory does our scalar-concentration ratio $r_{\langle \tilde{c} \rangle}$ show a slightly steeper decrease than that in the comparison simulation. This might be attributed to small differences in the very sensitive determination of the scalar trajectory and the coordinate transformation $x \rightsquigarrow \xi$ derived from it. Because the mapping $\xi = \xi(x)$ of the scalar trajectory at a downstream location is dependent on upstream information, potential deviations between the trajectory and the mapping of both simulations accumulate farther downstream. This could cause a small but visible difference between the mapping in our simulation and the comparison simulation, and thus a steeper decay rate in our simulation. Note, however, that the branch point, where the centerline maximum begins to deviate from the cross-sectional maximum, is predicted at about the same location in both simulations.

The maximum contravariant velocity $r_{\langle \tilde{u}_\xi \rangle}$ in Fig. 11c also decays with a power law, but faster than the maximum passive-scalar concentration (literature states an exponent of $k \approx -1.9$ [11]). However, the decay begins later, at $\xi \approx 1.7$, and does not exhibit the decreasing slope farther downstream as observed for the passive-scalar concentration. When considering all transverse locations, the agreement of our data to those of Yuan [11] is excellent at all positions. Because of the slight asymmetry in our data (cf. Fig. 9), the velocity maxima downstream of $\xi \gtrsim 4$ lie somewhat off the center plane. This yields a slightly faster decay of our centerline decay, whereas no considerable deviation (i.e., no significant off-centerline effect) is visible in the comparison simulation.

E. Flow Development Within Jet Nozzle

We now study the evolution of the mean flowfield within the jet nozzle by comparing it to the mean pipe flow of the precursor simulation. This allows one to assess the sufficiency of our nozzle length $L_{nozzle} = 5D$ (cf. Fig. 1), but also provides information about the potential adequacy of Dirichlet inlet conditions for the jet in the orifice plane $z = 0$. This "plug-flow" boundary condition is often found in JICF simulations using codes of high numerical accuracy (i.e., employing implicit finite difference or spectral methods). Their smaller geometrical flexibility does usually not allow one to incorporate the physical jet nozzle in the computational domain. Thus, as an approximation, suitable flow conditions are prescribed in the intersecting plane of nozzle and boundary-layer wall $z = 0$.

In the following, we consider the axial development (i.e., in z direction) of the mean flowfield within the jet nozzle $\langle \cdot_{nozzle} \rangle_t(x, y, z)$ in planes $z = $ const. To study the deviation $d(q, x, y, z)$ of a

quantity q from the mean inflow conditions, we subtract the time- and axially averaged flowfield of the precursor pipe simulation $\langle q_{pipe} \rangle_{t,z}(x, y)$,

$$d(q, x, y, z) := \langle q_{nozzle} \rangle_t(x, y, z) - \langle q_{pipe} \rangle_{t,z}(x, y) \qquad (5)$$

Figure 12 shows three measures derived from the flow deviation $d(q, x, y, z)$ for five quantities $q \in \{\langle \tilde{u} \rangle, \langle \tilde{v} \rangle, \langle \tilde{w} \rangle, \langle \tilde{p} \rangle, \langle \tilde{c} \rangle\}$ in dependence of the axial coordinate z: the maximum $d_{max}(q, z)$ and minimum $d_{min}(q, z)$ of d, as well as its rms value $n(q, z)$,

$$d_{max}(q, z) := \max_{x,y}[d(q, x, y, z)]$$

$$d_{min}(q, z) := \min_{x,y}[d(q, x, y, z)]$$

$$n(q, z) := \sqrt{\frac{\int_x \int_y d(q, x, y, z)^2 \, dx \, dy}{\int_x \int_y dx \, dy}} \qquad (6)$$

The general result is the same for all quantities except for the pressure, which assumes a special role. Deviations from the inlet profiles stay small along the majority of the nozzle downstream of its inlet, until $z \approx -1$ shortly below the orifice. Note that the symmetry of the mean flowfield yields an approximately mirrored development of the minimum and maximum deviations of the spanwise velocity $\langle \tilde{v} \rangle$. Those extreme values occur near the lateral edges of the nozzle, that is, near the points $[x, y, z]^T = [0, \pm 0.5, z]^T$.

The entrainment of boundary-layer fluid into the jet nozzle (at its upstream edge, see Fig. 6d) can be observed in the plot for the passive-scalar concentration, Fig. 12e. Whereas (as expected) both the maximum and minimum deviations stay very small downstream of the nozzle inlet (i.e., the nozzle contains pure jet fluid), the minimum deviation falls rapidly downstream of $z \approx -0.6$ due to the mixing of jet fluid with boundary fluid. In the inlet plane, the minimum deviation decreases to $d_{min} \approx -0.7$, that is, $\langle \tilde{c} \rangle_{min} \approx 0.3$. This means that the entrainment of the boundary layer results in a local predominance of the crossflow fluid in the orifice.

Because the pressure decreases overall along the nozzle due to friction, it cannot be expected to stay close to its initial profile in the inlet plane. Additionally, the precursor pipe simulation, which produces the inlet boundary condition, is decoupled from the main JICF simulation (see Sec. II), so that the prescribed pressure is generally not at the physically correct level for the jet nozzle. The pressure within the nozzle is influenced by the boundary-layer pressure downstream. This means that, due to the pressure loss along the nozzle caused by friction, the inlet plane of the nozzle exhibits a higher pressure than the boundary layer. This pressure level in the nozzle inlet due to the upstream influence of the boundary layer is slightly higher than the pressure that is prescribed from the independent precursor pipe simulation.

This small physical inconsistency (which cannot easily be avoided with the present compressible simulation approach in the subsonic
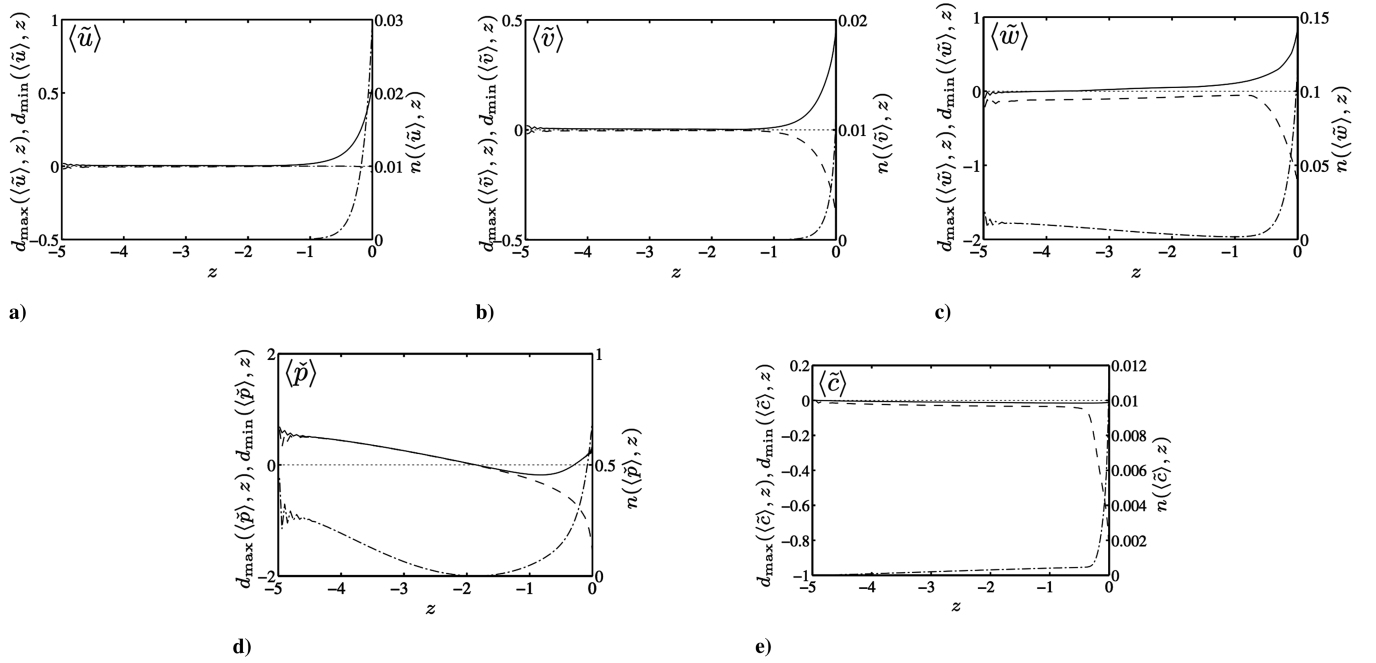
Fig. 12   Flow development within jet nozzle: a) streamwise velocity $\langle \tilde{u} \rangle$, b) spanwise velocity $\langle \tilde{v} \rangle$, c) vertical (axial) velocity $\langle \tilde{w} \rangle$, d) pressure $\langle \check{p} \rangle$, and e) passive-scalar concentration $\langle \tilde{c} \rangle$. Solid lines indicate maximum $d_{max}(q, z)$, dashed lines indicate minimum $d_{min}(q, z)$ (both left scale), and dashed-dotted lines indicate rms $n(q, z)$ (right scale) of deviation $d(q, x, y, z)$ of local mean flowfield $\langle q(x, y, z) \rangle_t$ within nozzle from mean pipe flow in planes $z = $ const.

flow regime) shows up in Fig. 12d as slight numerical oscillations near the inlet plane $z = -5$. They are most notable for the pressure, but also visible more weakly in the velocity components in Figs. 12a–12c. As apparent, they decay fast (within the first $0.3D$–$0.4D$ downstream from the inlet plane) and do not exhibit an adverse effect on the downstream flow development. Furthermore, the pressure is almost homogeneous in cross sections $z = $ const, because both the pressure maxima and minima are practically identical downstream of the inlet. As mentioned, they decrease until their intersection with the abscissa at $z \approx -1.9$. This coincides with the location of the minimum rms deviation $n \approx 0$, that is, the pressure in the nozzle has decreased to the level in the precursor pipe simulation. Downstream, the rms deviation increases steeply, and the maximum and minimum pressures follow different developments. The minimum decreases continually faster, whereas the pressure maximum sinks slightly more, but then increases somewhat for $z \geq -0.9$.

F.   Velocity and Passive-Scalar-Concentration Profiles in Center Plane

To allow for a quantitative comparison of our LES results with the incompressible reference simulation [11] and experiment [5], vertical profiles of the mean flowfield in the center plane are depicted at four different streamwise positions in Fig. 4. The first series of pictures, Figs. 4a–4d, shows the average velocity magnitude $\langle |\tilde{\mathbf{u}}| \rangle$. The overall agreement with the reference data is quite good. The first local minimum fits the experimental data better in our LES than in the one of Yuan [11]. In the next row of figures, 4e–4h, the normalized rms fluctuations of the velocity magnitude $|\tilde{\mathbf{u}}|_{rms}/\langle |\tilde{\mathbf{u}}| \rangle$ are plotted. Again, our LES generally reproduces the comparison results well.

The passive-scalar concentration $\langle \tilde{c} \rangle$ in Figs. 4i–4l exhibits excellent agreement for $x = 0$. Farther downstream, the value of the scalar-concentration peak is generally too low, but still comparable to the data of Yuan [11]. His parameter studies revealed a rising scalar concentration with increasing Reynolds number. As the Reynolds number in the measurements [6] is more than 4 times as high as in the current computations, the agreement should improve when adjusting the Reynolds number to the conditions of the experiment.

Figures 4m–4p depict the rms fluctuations of the scalar concentration $\tilde{c}_{rms}$. The overall agreement with experiment and computation is reasonable, and the positions and magnitudes of the peaks are also reproduced quite well. For the scalar intermittency

$\check{\gamma}$ in Figs. 4q–4t, no experimental data are available. Again, we observe good agreement with the results of Yuan [11] for all streamwise positions. However, as another consequence of a potential higher degree of scalar dissipation in our simulation, our curves generally show somewhat less steep gradients at all positions.

V.   Instantaneous Flowfield

A.   Three-Dimensional Flowfield and Vortex Structures

The isocontour of the passive-scalar concentration in Fig. 13a gives a good impression of the unsteady and irregular flow state caused by the mixing of the two streams. The roll up and breakdown of the jet shear layer is also observable: the initially smooth contour surface above the jet exit shows a regular pattern of ripples (see marker 1) after a distance along the jet trajectory of approximately one jet hole diameter. A few diameters farther downstream (cf. marker 2), the structure changes to an irregular form, which coincides with the breakup of the shear-layer vortices.

Figures 13b and 13c depict an isocontour of the instantaneous vortex-identification quantity $\check{\lambda}_2$. The (arbitrarily selected) contour value is lower in Fig. 13c than in Fig. 13b, thus fewer and only the more pronounced vortex structures are visible there. Similar to the flow around a wall-mounted cylinder, a horseshoe vortex (3) wraps around the jet exit hole. When varying the isocontour value of $\check{\lambda}_2$ or considering vector representations of the velocity fields near the jet nozzle, a series of circular vortices with alternating orientation is visible. However, due to the selected isocontour value, just one structure appears. The mentioned shedding of shear-layer vortices (1) from the upstream edge of the jet nozzle is directly visible in Fig. 13b. After a few jet diameters along the trajectory (cf. marker 2) they lose their distinct appearance. This marks the location of their breakup, which was already observed in the isocontour of the passive-scalar concentration in Fig. 13a.

The spanwise roller at the downstream edge of the nozzle is largely visually obstructed by the other vortex structures in this region. However, the legs of the horseshoe vortex (4) are clearly visible as elongated streamwise vortices in the boundary layer downstream of the jet nozzle. As they travel downstream, they are eventually rotated into an upright position, as clearly evident from marker (5) in Fig. 13c. Together with the wake vortices (6), which are shed when the boundary layer experiences an adverse pressure gradient while moving around the jet core, they form the vertical traveling vortices
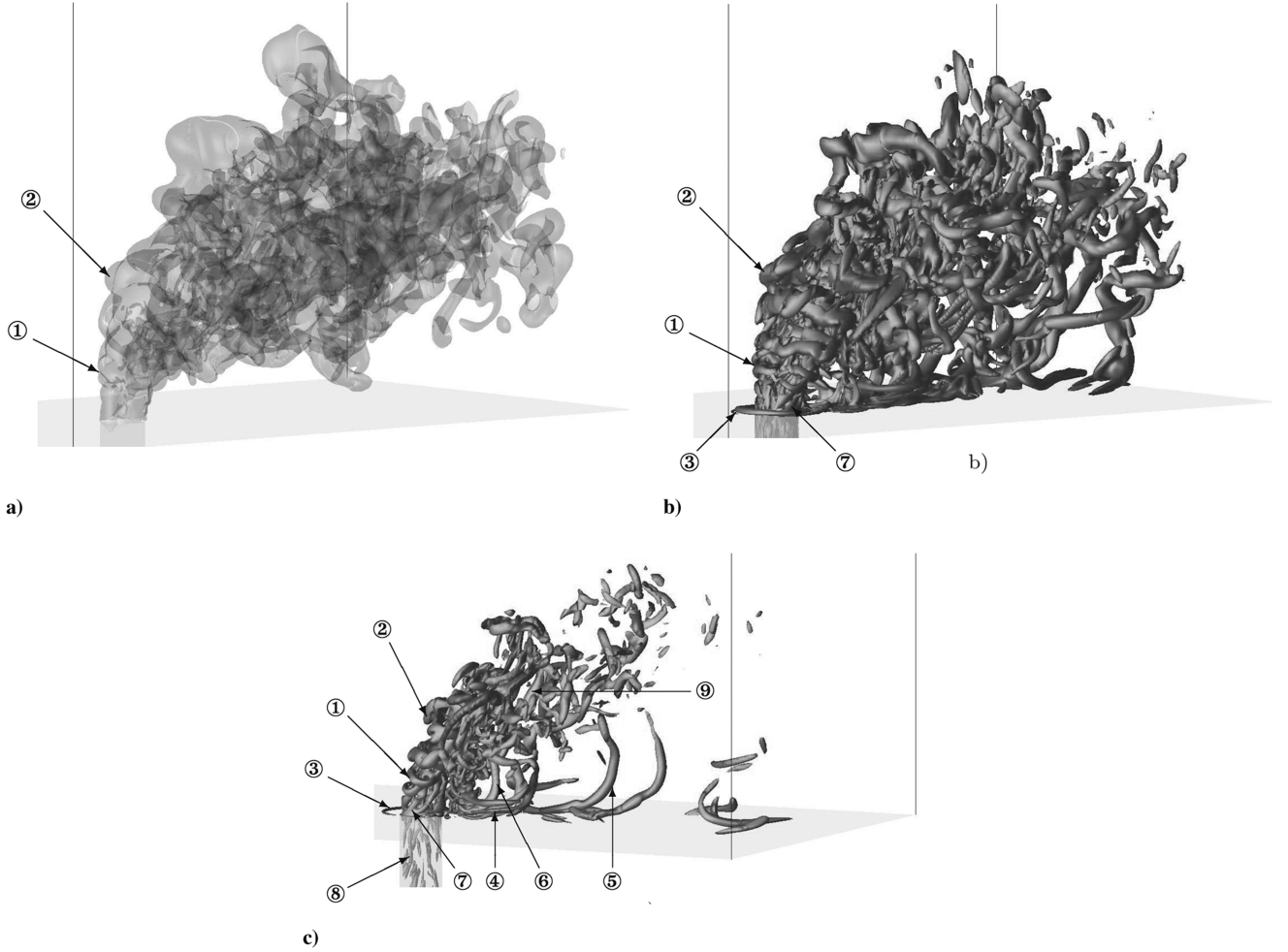
Fig. 13 Visualizations of the instantaneous flowfield: a) transparent isocontour of the passive-scalar concentration (level $\tilde{c} = 0.1$), b–c) vortex-identification criterion $\breve{\lambda}_2$ at two different isocontour levels and viewing angles.

downstream of the jet core. The shedding process is even amplified by the vorticity induced from the hanging vortices (7) in the region close to the jet exit.

Note that the counter-rotating vortex pair is not visible as a distinct vortex structure in the instantaneous flowfield. However, the rich array of smaller flow structures along the jet trajectory is moving in a counter-rotating manner. The streaky structures originating from the turbulent pipe flow (8) mainly show up as elongated vortices aligned with the jet trajectory (9) farther downstream.

B. Flow and Passive-Scalar-Concentration Contours in Center Plane

In Fig. 14, we consider contours of the instantaneous flowfield in the center plane at the same instant of time as in Fig. 13. The instantaneous velocity magnitude $|\tilde{\mathbf{u}}|$ in Fig. 14a reveals the highly unsteady character of the velocity field downstream of the jet exit. The series of circular regions of low velocity magnitude above the upstream edge of the jet exit hole are a sign of shear-layer vortices shedding from the jet exit. In the instantaneous pressure field in Fig. 14d, those vortices are visible as an alternating pattern of circular high- and low-pressure zones. Note the blob of high velocity magnitude at $z \approx 2.5$, which is about to separate from the jet core below. When compared with the instantaneous passive-scalar concentration in Fig. 14c, this corresponds to an almost isolated region with high scalar-concentration levels. Here the shear-layer vortices seem to induce a movement that leads to the entrainment of boundary-layer fluid with low vertical velocity into the ejected jet core.

The instantaneous spanwise velocities $\tilde{v}$ in Fig. 14b are remarkably high, with levels nearly twice as large as the freestream velocity. The maximum values occur above the downstream edge of

the jet nozzle and are induced by the hanging vortices. High spanwise velocities are also observable along the jet trajectory as a consequence of the counter-rotating vortex pair. The vertically oriented zones of high spanwise velocity are caused by the wake vortices. This is especially evident when comparing their form and locations to Fig. 13c.

The roll up of the jet shear layer on its upstream edge can be very clearly recognized in the contour of the passive-scalar concentration $\tilde{c}$ (Fig. 14c). The upstream boundary of high scalar-concentration levels shows three distinct vortical patterns. Two much smaller ones can also be spotted on the downstream boundary. Note that significant concentration levels occur even in regions very far away from the jet trajectory. This is a typical consequence of the strong vortex systems near the jet nozzle and especially the CVP along its trajectory, which leads to an extensive transport of jet fluid away from its core.

C. Oscillation of Jet and Vortex Shedding

Animations of the instantaneous passive-scalar field such as depicted in Fig. 13 reveal that the ejected jet body above the wall does not stay at a fixed position according to its time-averaged location, but rather it oscillates considerably in all three spatial dimensions. This low-frequency wagging process can be analyzed by defining the center of the three-dimensional passive-scalar field similarly to the center of gravity of a density distribution:

$$\mathbf{r}(t) = [r_x(t), r_y(t), r_z(t)]^T$$
$$:= \frac{\int_\Omega [x, y, z]^T \bar{\rho}(x, y, z, t) \tilde{c}(x, y, z, t) \, dV}{\int_\Omega \bar{\rho}(x, y, z, t) \tilde{c}(x, y, z, t) \, dV} \tag{7}$$
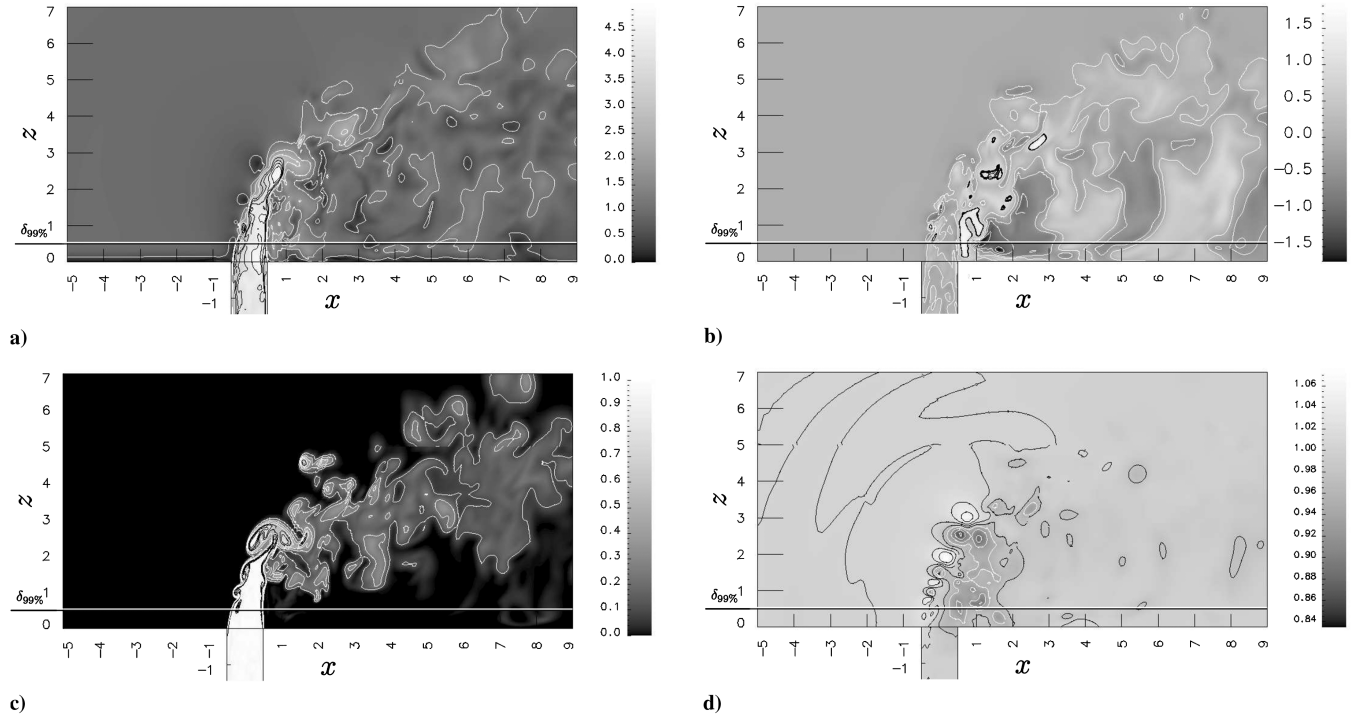
Fig. 14   Visualization of instantaneous flowfield in the center plane $y = 0$: a) velocity magnitude $|\breve{u}|$, b) spanwise velocity $\tilde{v}$, c) passive-scalar concentration $\tilde{c}$, and d) normalized pressure $\breve{p}/\breve{p}_{\infty}$. Contour legend as in Fig. 6.

The volumetric domain Ω denotes all fluid elements above the flat plate (i.e., $z > 0$). Of course, the streamwise (and, to a lesser degree, the vertical) location of this measure is dependent on the streamwise length of the computational domain and can only be considered in a qualitative way. The temporal development of the three center-point components is shown in Fig. 15a. Unfortunately, the limited amount of (very memory-intensive) three-dimensional instantaneous flowfields necessary for this analysis does not allow for an accurate assessment of dominant frequencies. We feel, however, that this time interval is large enough for a qualitative illustration of the wagging process and some preliminary quantitative statements. The streamwise component of the center point r_x fluctuates around a value of roughly 5.5 with a quite regular oscillation pattern. About three periods can be observed in the investigated time interval of 21 time units, which yields a Strouhal number of $St_{\mathrm{JICF}} = fD/\tilde{u}_{\infty} \approx 0.14$ (f being the dimensionless frequency). This suggests that the streamwise wagging of the jet is connected to the formation of wake vortices, which were found to exhibit a Strouhal

number of $St_{\mathrm{JICF}} = 0.1$–0.2 [38,39], similar to vortex shedding around a cylinder [40] ($St \approx 0.21$ based on freestream values and the cylinder diameter).

The vertical component r_z weakly shows features of the behavior of the streamwise component r_x. But because it is generally falling (from about $r_z \approx 4$ to $r_z \approx 3.5$) in the observed time frame, there seem to be other effects that influence the vertical jet position at a considerably larger timescale. The same applies to the behavior of the spanwise center-point component r_y.

Another characteristic periodic process is the roll up of the jet shear layer above the upstream edge of the orifice, resulting in the formation of shear-layer (Kelvin–Helmholtz) vortices. We captured the temporal development of the instantaneous flowfield at a position in the shedding region, which was determined from flow animations such as Fig. 14. The characteristic frequencies associated with the jet shear-layer roll up are clearly visible from the energy-density spectra of most fluctuating flow quantities. An example is the spectrum of the vertical-velocity fluctuations in Fig. 15b, which exhibits three
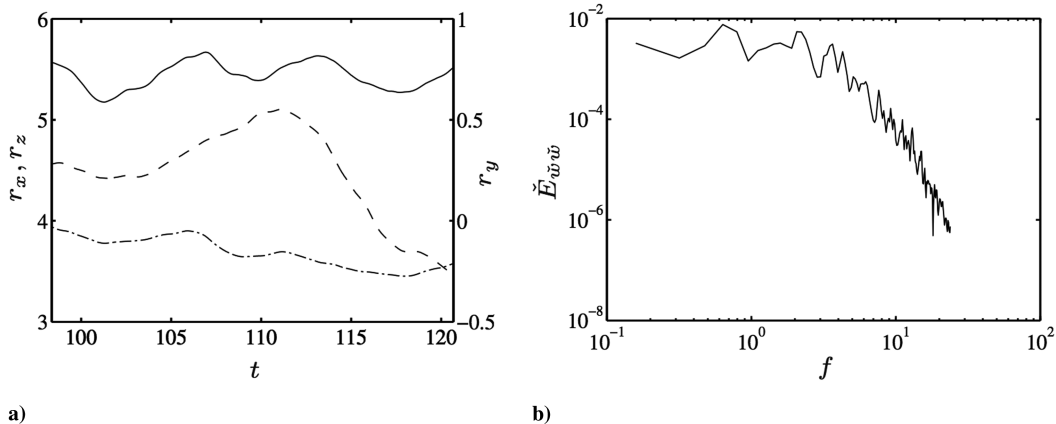

Fig. 15   Quantification of jet oscillation and vortex shedding: a) temporal development of center point of passive-scalar concentration $[r_x, r_y, r_z]^T$ above flat wall [solid line is r_x (left scale), dashed line is r_y (right scale), dashed-dotted line is r_z (left scale)]; b) energy-density spectrum $\breve{E}_{\tilde{w}\tilde{w}}$ of the fluctuations of the vertical-velocity component $\tilde{w}$ in a point above the orifice ($[x, y, z]^T \approx [-0.25, 0, 0.9]^T$).

distinct peaks at frequencies f corresponding to jet Strouhal numbers of $St_{jet} = fD/\tilde{u}_{CL} \approx 0.16$, 0.55, and 0.9 (with the jet centerline velocity $\tilde{u}_{CL}$).

Although this result is in qualitative agreement with the recent experimental findings of Megerian et al. [41] (cf. Fig 8c), there are some notable differences. First, the experimentally observed peaks are considerably spikier and more distinct than in the present simulation. Furthermore, their frequencies lie about 30% above the present values. Finally, at a distance of about one nozzle diameter above the orifice, Fig. 8c in [41] shows only a single peak at a Strouhal number equivalent to the middle peak at locations farther away from the nozzle. Only somewhat downstream, three peaks are visible, as in Fig. 15b.

These differences could potentially be due to deviations in the sampling location, the flow parameters (the present simulation uses a different blowing ratio, Reynolds number, and boundary-layer thickness), and jet outflow profiles. Whereas the jet profile in [41] was close to a top-hat profile, a fully developed turbulent pipe-flow profile (distorted by the crossflow as investigated in Sec. IV.E) is present in our simulation. This difference could exhibit a considerable effect on the characteristics of the shear-layer roll up, as indicated by the wide range of dominant frequencies from literature for quite similar blowing ratios (also cf. Table 1 in [41]).

Finally, note that earlier literature at similar flow parameters cites jet Strouhal numbers in the range of $St_{jet} \approx 0.5–0.8$ [42], 0.65 [1], or 0.7–0.75 [39] as frequencies for the shear-layer roll up. This is in quite good agreement with the frequency of the middle peak in Fig. 15b, which is equivalent to the primary roll-up frequency at locations close to the orifice in Fig. 8c of [41].

VI. Conclusions

The evolution of a round turbulent jet issuing perpendicularly into a laminar boundary-layer crossflow has been numerically investigated using the compressible multiblock finite volume code NSMB at a jet-to-crossflow momentum ratio of 3.3 and a jet Reynolds number of 6930. The flow parameters have been chosen according to those of the previous incompressible simulations of Yuan [11] and the experiments of Sherif and Pletcher [5], except for the Mach number, which was kept at the low value of 0.2 to maintain comparability and to avoid excessive computational costs due to very small time steps. The subgrid scales were accounted for by the approximate deconvolution model [18,19] for LES. Turbulent inflow data for the jet nozzle were generated with a simultaneously running simulation of turbulent pipe flow. This pragmatic method was found to work well and only introduce minor locally confined inaccuracies (due to small deviations in the pressure level) at this low Mach number.

The simulation approach and the simulation results were validated by a comparison with the data from the LES of Yuan [11] and experiments of Sherif and Pletcher [5]. Good agreement was not only found for the vertical first- and second-order profiles of the velocity magnitude and passive-scalar concentration, but also for more sensitive derived quantities such as the jet trajectory and the jet spreading, as well as the decay of concentration and momentum along its trajectory. This demonstrates the applicability and adequacy of the present pragmatic simulation approach and the inflow-generation method for the turbulent jet nozzle.

In contrast to previous literature, jet spreading data are also presented for the region close to the orifice. Three distinct regimes are visible in these data. In the zone of the jet core, the jet spreads quickly. At the closing of the jet core, the spreading almost stagnates. Finally, about four nozzle diameters downstream of the orifice, the typical almost-constant spreading begins at a considerably lower rate than initially.

The most prominent mean-flow features were clearly visualized with streamlines, as well as various cross sections through the computational domain. The development of the jet along its trajectory was documented with cuts normal to the jet trajectory. The data show the typical flow structures for this parameter range.

The investigation of the mean flow within the nozzle showed that the upstream influence of the crossflow into the nozzle is limited to about one nozzle diameter below the orifice. From the nozzle inlet until that region, the mean-flow profile within the nozzle is essentially unchanged from the precursor pipe simulation. One nozzle diameter below the orifice, it is, however, subject to considerable changes due to the influence of the crossflow. At this moderate blowing ratio, the entrainment of crossflow fluid into the jet nozzle is rather limited and restricted to a small region below the upstream edge of the orifice. Overall, the analysis indicates that the nozzle length of five nozzle diameters seems to be sufficient and could probably be shortened to about half that value. Furthermore, assuming a symmetrical outflow profile for the jet in numerical plug-flow simulations of a jet in crossflow does not seem to adequately model the influence of the jet nozzle.

The features of the instantaneous flowfield were illustrated in two- and three-dimensional snapshots. In contrast to the stationary vortices recognizable from the mean-flow visualizations, this allows one to see the moving vortex structures. For instance, the Kelvin–Helmholtz shear-layer instability above the upstream edge of the orifice, as well as the closing of the jet core and the increased entrainment of crossflow fluid into the jet body, are clearly visible phenomena.

The frequencies associated with this shear-layer instability were compared with results from literature. Although the corresponding peaks in the power spectra of the velocity fluctuations are somewhat broader and less distinct than observed in experiments, their locations are reasonably in the range of the reference data.

Three-dimensional animations of the flow data showed a periodic spatial oscillation (wagging) of the ejected jet core. This was quantified with the temporal variation of the center point of the passive-scalar concentration. Although the limited amount of instantaneous flow data does not allow for a definitive analysis, a quite regular oscillation in the downstream direction is observable at a frequency roughly equivalent to the formation of wake vortices. The oscillations in the other two directions appear to occur at a much smaller timescale exceeding the available data. Overall, considerably more instantaneous data (at least the tenfold amount) will be necessary to make conclusive statements and assess the connection between the three-dimensional jet wagging and the vortex formation in the near field.

References

[1] Kelso, R. M., Lim, T. T., and Perry, A. E., "An Experimental Study of Round Jets in Cross-Flow," *Journal of Fluid Mechanics*, Vol. 306, Jan. 1996, pp. 114–144.
doi:10.1017/S0022112096001255

[2] Margason, R. J., "Fifty Years Of Jet In Cross Flow Research," *Computational and Experimental Assessment of Jets in Cross Flow*, AGARD Rept. CP-534, Nov. 1993.

[3] Andreopoulos, J., and Rodi, W., "Experimental Investigation of Jets in a Crossflow," *Journal of Fluid Mechanics*, Vol. 138, Jan. 1984, pp. 93–127.
doi:10.1017/S0022112084000057

[4] Andreopoulos, J., "On the Structure of Jets in a Crossflow," *Journal of Fluid Mechanics*, Vol. 157, Aug. 1985, pp. 163–197.
doi:10.1017/S0022112085002348

[5] Sherif, S. A., and Pletcher, R. H., "Measurements of the Flow and Turbulence Characteristics of Round Jets in Crossflow," *Journal of Fluids Engineering*, Vol. 111, June 1989, pp. 165–171.

[6] Sherif, S. A., and Pletcher, R. H., "Measurements of the Thermal Characteristics of Heated Turbulent Jets in Cross Flow," *Journal of Heat Transfer*, Vol. 111, No. 4, 1989, pp. 897–903.

[7] Fric, T. F., and Roshko, A., "Vortical Structure in the Wake of a Transverse Jet," *Journal of Fluid Mechanics*, Vol. 279, Nov. 1994, pp. 1–47.
doi:10.1017/S0022112094003800

[8] Smith, S. H., and Mungal, M. G., "Mixing, Structure and Scaling of the Jet in Crossflow," *Journal of Fluid Mechanics*, Vol. 357, Feb. 1998, pp. 83–122.
doi:10.1017/S0022112097007891

[9] Lim, T. T., New, T. H., and Luo, S. C., "On the Development of Large-Scale Structures of a Jet Normal to a Cross Flow," *Physics of Fluids*, Vol. 13, No. 3,.
doi:10.1063/1.1347960

[10] Su, L. K., and Mungal, M. G., "Simultaneous Measurements of Scalar and Velocity Field Evolution in Turbulent Crossflowing Jets," *Journal of Fluid Mechanics*, Vol. 513, Aug. 2004, pp. 1–45.
doi:10.1017/S0022112004009401

[11] Yuan, L. L., "Large Eddy Simulations of a Jet in Crossflow," Ph.D. Thesis, Stanford Univ., Stanford, CA, 1997.

[12] Yuan, L. L., and Street, R. L., "Trajectory and Entrainment of a Round Jet in Crossflow," *Physics of Fluids*, Vol. 10, No. 9, 1998, pp. 2323–2335.
doi:10.1063/1.869751

[13] Yuan, L. L., Street, R. L., and Ferziger, J. H., "Large Eddy Simulations of a Round Jet in Crossflow," *Journal of Fluid Mechanics*, Vol. 379, Jan. 1999, pp. 71–104.
doi:10.1017/S0022112098003346

[14] Schlüter, J. U., and Schönfeld, T., "LES of Jets in Crossflow and its Application to a Gas Turbine Burner," *Flow, Turbulence and Combustion*, Vol. 65, No. 2, 2000, pp. 177–203.
doi:10.1023/A:1011412810639

[15] Muppidi, S., and Mahesh, K., "Study of Trajectories of Jets in Crossflow Using Direct Numerical Simulations," *Journal of Fluid Mechanics*, Vol. 530, May 2005, pp. 81–100.
doi:10.1017/S0022112005003514

[16] Muppidi, S., and Mahesh, K., "Direct Numerical Simulation of Round Turbulent Jets in Crossflow," *Journal of Fluid Mechanics*, Vol. 574, March 2007, pp. 59–84.
doi:10.1017/S0022112006004034

[17] Cortelezzi, L., and Karagozian, A. R., "On the Formation of the Counter-Rotating Vortex Pair in Transverse Jets," *Journal of Fluid Mechanics*, Vol. 446, Nov. 2001, pp. 347–373.

[18] Stolz, S., and Adams, N. A., "An Approximate Deconvolution Procedure for Large-Eddy Simulation," *Physics of Fluids*, Vol. 11, No. 7, 1999, pp. 1699–1701.
doi:10.1063/1.869867

[19] Stolz, S., Adams, N. A., and Kleiser, L., "The Approximate Deconvolution Model for Large-Eddy Simulations of Compressible Flows and its Application to Shock-Turbulent-Boundary-Layer Interaction," *Physics of Fluids*, Vol. 13, No. 10, 2001, pp. 2985–3001.
doi:10.1063/1.1397277

[20] Vos, J. B., van Kemenade, V., Ytterström, A., and Rizzi, A. W., "Parallel NSMB: An Industrialized Aerospace Code for Complete Aircraft Simulations," *Parallel CFD Conference 1996*, North-Holland, Amsterdam, 1997, pp. 49–58.

[21] Vos, J. B., Rizzi, A., Corjon, A., Chaput, E., and Soinne, E., "Recent Advances in Aerodynamics inside the NSMB (Navier Stokes Multi Block) Consortium," AIAA Paper 98-0225, 1998.

[22] Ziefle, J., Stolz, S., and Kleiser, L., "Large-Eddy Simulation of Separated Flow in a Channel with Streamwise-Periodic Constrictions," AIAA Paper 2005-5353, 2005.

[23] Ziefle, J., Stolz, S., and Kleiser, L., "Large-Eddy Simulation of Separated Flow in a Channel with Streamwise-Periodic Constrictions," *AIAA Journal*, Vol. 46, No. 7, July 2008, pp. 1705–1718.
doi:10.2514/1.33891

[24] Poinsot, T. J., and Lele, S. K., "Boundary Conditions for Direct Simulations of Compressible Viscous Flows," *Journal of Computational Physics*, Vol. 101, No. 1, 1992, pp. 104–129.
doi:10.1016/0021-9991(92)90046-2

[25] Oosthuizen, P. H., and Naylor, D., *Introduction to Convective Heat Transfer Analysis*, WCB/McGraw–Hill, Burr Ridge, IL, 1999.

[26] Vos, J. B., Leyland, P., van Kemenade, V., Gacherieu, C., Duquesne, N., Lotstedt, P., Weber, C., Ytterström, A., and Saint Requier, C., NSMB Handbook 4.5, NSMB Consortium, Lausanne, Switzerland, 2001.

[27] Gacherieu, C., Collercandy, R., Larrieu, P., Soumillon, P., Tourette, L., and Viala, S., "Navier-Stokes Calculations at Aerospace Matra Airbus for Aircraft Design," Royal Aeronautical Society Paper 2.6.1, 2000.

[28] Viala, S., Amant, S., and Tourette, L., "Recent Achievements on Navier-Stokes Methods for Engine Integration," Council of European Aerospace Societies, Royal Aeronautical Society Paper 54, 2002.

[29] Mossi, M., "Simulation of Benchmark and Industrial Unsteady Compressible Turbulent Fluid Flows," Ph.D. Thesis No. 1958, Ecole Polytechnique Fédérale de Lausanne, Switzerland, 1999.

[30] Blaisdell, G. A., Spyropoulos, E. T., and Qin, J. H., "The Effect of the Formulation of Nonlinear Terms on Aliasing Errors in Spectral Methods," *Applied Numerical Mathematics*, Vol. 21, No. 3, 1996, pp. 207–219.
doi:10.1016/0168-9274(96)00005-0

[31] Kravchenko, A. G., and Moin, P., "On the Effect of Numerical Errors in Large Eddy Simulations of Turbulent Flows," *Journal of Computational Physics*, Vol. 131, No. 2, 1997, pp. 310–322.
doi:10.1006/jcph.1996.5597

[32] Coleman, G. N., Kim, J., and Moser, R. D., "A Numerical Study of Turbulent Supersonic Isothermal-Wall Channel Flow," *Journal of Fluid Mechanics*, Vol. 305, Dec. 1995, pp. 159–183.
doi:10.1017/S0022112095004587

[33] Ziefle, J., and Kleiser, L., "Large-Eddy Simulation of a Round Jet in Crossflow," AIAA Paper 2006-3370, 2006.

[34] Jeong, J., and Hussain, F., "On the Identification of a Vortex," *Journal of Fluid Mechanics*, Vol. 285, Feb. 1995, pp. 69–94.
doi:10.1017/S0022112095000462

[35] Chen, C. J., and Rodi, W., *Vertical Turbulent Buoyant Jets*, Pergamon Press, Oxford, 1980.

[36] Ricou, F. P., and Spalding, D. B., "Measurements of Entrainment by Axisymmetrical Turbulent Jets," *Journal of Fluid Mechanics*, Vol. 11, No. 1, 1961, pp. 21–31.
doi:10.1017/S0022112061000834

[37] Kamotani, Y., and Greber, I., "Experiments on a Turbulent Jet in a Cross Flow," *AIAA Journal*, Vol. 10, No. 11, 1972, pp. 1425–1429.
doi:10.2514/3.50386

[38] Fric, T. F., "Structure in the Near Field of the Transverse Jet," Ph.D. Thesis, California Inst. of Technology, Pasadena, CA, 1990.

[39] Rudman, M., "Simulation of the Near Field of a Jet in a Cross Flow," *Experimental Thermal and Fluid Science*, Vol. 12, No. 2, 1996, pp. 134–141.
doi:10.1016/0894-1777(95)00089-5

[40] Roshko, A., "On the Development of Turbulent Wakes from Vortex Streets," Ph.D. Thesis, California Inst. of Technology, Pasadena, CA, 1952.

[41] Megerian, S., Davitian, J., Alves, L. S. de B., and Karagozian, A. R., "Transverse-jet shear-layer instabilities. Part 1. Experimental Studies," *Journal of Fluid Mechanics*, Vol. 593, 2007, pp. 93–129.
doi:10.1017/S0022112007008385

[42] Shapiro, S., King, J., M'Closkey, R. T., and Karagozian, A. R., "Optimization of Controlled Jets in Crossflow," *AIAA Journal*, Vol. 44, No. 6, 2006, pp. 1292–1298.
doi:10.2514/1.19457